ELSEVIER

Mechanics of Materials 31 (1999) 331–350

MECHANICS OF MATERIALS

Shear-lag model for failure simulations of unidirectional fiber composites including matrix stiffness

Irene J. Beyerlein [a,*], Chad M. Landis [b]

[a] *Center for Materials Science, Mail Stop G 755, Los Alamos National Laboratory, Los Alamos, NM 87545, USA*
[b] *Department of Mechanical and Environmental Engineering, University of California, Santa Barbara, CA 93106, USA*

Received 13 July 1998; received in revised form 16 November 1998

Abstract

In this paper, we develop a shear-lag model and an influence superposition technique to quickly compute the stresses and displacements in 2D unidirectional fiber composites in response to multiple fiber and matrix breaks. Unlike previous techniques, both the fiber and matrix are able to sustain axial load, and the governing shear-lag equations are derived based on the principle of virtual work and the finite element method. The main advantages of influence superposition techniques are that computation is tied to the amount of damage, rather than the entire volume considered and discretization is not needed, removing any uncertainties associated with meshing. For illustration, we consider a row of N (up to 301) contiguous fiber breaks and highlight important influences that N and the matrix-to-fiber stiffness ratio, $\rho = E_m A_m / E_f A_f$, have on stress redistribution. Comparisons with the Mode I plane orthotropic linear elasticity solution are favorable for both shear and axial tensile stresses. The best applications for such techniques are as numerical micromechanics tools in large-scale simulation codes of failure in fibrous composites. The present study is an important prerequisite for simulations and modeling of random fracture patterns, as would naturally develop in a real composite. Arbitrarily misaligned breaks are no more complicated to compute, and we reserve analyses of such cases to future simulation work involving random fiber strengths.

Keywords: Fiber composites; Shear-lag analysis; Axial matrix stiffness; Stress concentrations; Plane linear elasticity; Numerical simulation

1. Introduction

This work develops a shear-lag model for computing stresses and displacements in composites consisting of parallel continuous fibers in a planar array, separated by a matrix material. This model is capable of calculating both the tensile and shear stresses in the matrix, as well as the tensile stresses in the fiber in response to multiple fiber breaks in any 2D arrangement. Such models are developed for use in large-scale breakdown simulations of fiber composites to address fundamental issues regarding materials manufacturing and design. Though failure modes and mechanisms involved in fiber composite breakdown are likely to vary with a particular composite material system, fiber breaks and localized crack formation are most often prevalent. Interactions between these breaks alone can lead to very complex stress and displacement fields. Combining finite element theory and influence

* Corresponding author. E-mail: irene@lanl.gov.

0167-6636/99/$ – see front matter
PII: S0167-6636(98)00075-1

superposition concepts, the shear-lag model developed here will be able to compute these fields while cutting computational requirements by a few orders of magnitude and eliminating the need for discretization.

In previous work, influence superposition techniques were developed to handle multiple fiber breaks in any configuration in unidirectional fiber composites, with separate algorithms for (i) elastic matrices (Sastry and Phoenix, 1993; Zhou and Curtin, 1995; Landis et al., 1998a, b), (ii) sliding or debonding interfaces (Suemasu, 1984; Beyerlein and Phoenix, 1996; Landis and McMeeking, 1998), and (iii) viscoelastic matrices (Beyerlein et al., 1998a). These techniques have been built upon either the Hedgepeth (1961) shear-lag model for 2D and 3D multifiber composites, or on finite element-based shear-lag theory for 3D composites. Thus far, these techniques, with the exception of Landis and McMeeking (1998), assume that the fibers carry all the axial load, and the matrix material only transmits shear between the fibers. Based on these assumptions alone, it is generally accepted that these methods will be most accurate when the fiber volume fraction V_f and the fiber-to-matrix moduli ratio E_f/E_m are high, i.e., $E_f V_f \gg E_m(1 - V_f)$. However, many composites of current interest, such as metal matrix (MMCs) and some low V_f polymer matrix composites (PMCs), do not fall in this category. Also, when the matrix is assumed not to sustain axial tensile forces, these shear-lag models cannot differentiate between a transverse matrix crack extending from the fiber break all the way to the next fiber versus no crack extension into the matrix. Especially in composite systems where the matrix strain-to-failure is lower or comparable to that of the fiber, as in some MMCs and CMCs, the effects of matrix cracking are extremely important. The method we develop in this work, however, will differentiate between these cases. As in the shear lag models of Landis and McMeeking (1998), the present one incorporates the influences of matrix axial stiffness based on the principle of virtual work by using the finite element method.

The fundamental concepts behind *influence superposition techniques* are to obtain analytical solutions for the influence of a 'unit' failure on the stress and displacement fields and then use a weighted superposition technique to obtain the solution for the full problem. The unit solution developed in this work allows for the matrix to sustain a portion of the tensile stress and in dimensionless form, depends only on $\rho = E_m A_m / E_f A_f$.

1.1. Theoretical background

There exists a rich variety of composite systems which could benefit from such shear-lag stress analyses. On the one hand, many concerns arise in utilization of shear-lag models because of their inability to account for the influence of all stress components. On the other hand, its simplicity relative to more complete, full field stress analyses have attracted several authors to extend the multifiber shear-lag model of Hedgepeth to include many features for both planar (2D) and regular 3D arrangements of fibers. The original Hedgepeth model assumes that the matrix and fiber were both linearly elastic and well-bonded, but later Hedgepeth and co-workers (Van Dyke and Hedgepeth, 1969; Hedgepeth and Van Dyke, 1967) included effects of an elastic-perfectly plastic matrix or complete interfacial failure. Also for simplicity, their analytical solutions were derived for stress concentrations immediately adjacent to a single break.

Many followed with similar intentions allowing for one or a combination of features: (i) yielding matrices (Goree and Gross, 1980; Zweben, 1974), (ii) interfacial debonding (Nairn, 1988; Ochiai et al., 1991), (iii) for matrices that support a portion of the tensile stress (Ochiai et al., 1991; Fukuda and Kawata, 1976; Rossettos and Shishesaz, 1987; Zeng et al., 1997) or transverse stresses (Goree and Gross, 1980; Eringen and Kim, 1973; Mukunda and Dharani, 1993) and (iv) for hybrid composites (Fukuda and Chou, 1983). In some of these cases, improvements have led to analytical difficulties or the need for extensive numerical computation. In virtually all cases, the restriction to consider just a single break and a small row of breaks or a small region of fibers is needed to make the problem tractable. In the latter case, reliable predictions

depend on the size of this region relative to the number of aligned breaks in the cluster. Moreover, dependences of the numerical solutions on a majority of the fiber and matrix properties are not conveniently removed through normalizations, so that their calculations only apply for a given set of composite parameters. Also in some of these models, predictions from these modified versions do not reduce to those of the Hedgepeth shear-lag model when their respective refinements are removed.

1.2. Experimental measurements

The motivation for the development of this computational tool, which allows the matrix to sustain tensile stresses, are (i) recent in situ experimental measurements of the axial stress in fibers and observations of damage development due to a single fiber break and (ii) to widen the range of material systems which can be treated using the shear-lag model.

Two peizospectroscopy techniques, chromium fluorescence (He and Clarke, 1995) and micro-Raman spectroscopy (MRS), (Schadler et al., 1996), have advanced the state of the art in the in situ measurement of stresses and strains in small diameter fibers and interfaces in model composites. To date, it has been established through many peizospectroscopy experiments with high V_f model composites that the shear-lag approach yields realistic and useful fiber and matrix stress results (He et al., 1998; Beyerlein et al., 1998b). These measurements are usually performed using model composites, where 5–10 fibers are placed in parallel in a planar array, or in larger specimens, where measurements are possible on the surface.

Several recent studies using peizospectroscopic techniques have shown that as the interfiber spacing increases, the stress concentrations in the immediate neighboring fiber decreases (Wagner et al., 1996; van den Heuvel et al., 1997; He et al., 1998; Beyerlein et al., 1998b). Not surprisingly, shear-lag models that do not consider axial matrix stiffness have been unsuccessful in interpreting this data. In such model composites, the fiber spacing can be much greater than the fiber diameter or non-uniform within the specimen, or there can be an excess of matrix in the thickness direction perpendicular to the plane of the fibers. In these cases, matrix tensile stresses are significant, and specifically non-uniform fiber spacing can alter load transfer even when the matrix is assumed to have zero stiffness (Landis and McMeeking, 1998). The shear-lag model and influence superposition technique developed here is designed to overcome this deficiency and thus improve interpretation of peizospectroscopic data obtained in such model composites. However, due to the inconsistency between the present model geometry and that of experimental specimens, we will reserve comparison with experimental data for future work. Nevertheless, it should be kept in mind that stress concentrations measured in planar model composites with few fibers and high V_m or on the surface may overestimate those found in real (3D) composites with the same local fiber spacing, due to the reduction in number of nearest neighbors and modification of the long range load transfer.

In composites of high V_f, which are of commercial interest, shear-lag models have proven to capture most of the features that can be experimentally measured at the length scale of a fiber diameter (He et al., 1998; Beyerlein et al., 1998b). Clearly, there is still plenty of room for refinement, such as the addition of axial load carrying capability, transverse stresses in the matrix and interfacial debonding or sliding, with only moderate increases in computational cost. Considering the enormous computational demands for simulations involving thousands of breaks, which is needed to capture large scale statistical features, one cannot afford to expend several degrees of freedom per break. In the following sections, the axial load carrying capability of the matrix is built into a 2D shear-lag model and incorporated into a influence superposition technique with the same multiple break capabilities (not only fiber breaks, but now matrix breaks, too) and efficiency of previous ones. The shear-lag model developed here approaches results predicted by the Hedgepeth shear-lag model as $E_m V_m$ goes to zero.

2. Governing shear-lag equations and normalizations

Consider a region within a 2D, unidirectional fiber composite with evenly spaced fibers as shown in Fig. 1. The analysis assumes that the thickness, t, in the out-of-plane direction, is the same for the fibers and matrix. The width of each matrix region is W, and the width of the fibers is D. In the model, the transverse displacements of the system and the shear deformation of the fibers are neglected. Therefore, the relevant material properties are the axial Young's modulus of the fibers and matrix, E_f and E_m, and the axial shear modulus of the matrix, G_m. As indicated on Fig. 1, both the fiber and matrix are subjected to the same far field strain ε.

The first step in the analysis is to create a finite element model of the composite system. Fig. 2 shows a segment of the mesh, representing a repeating cell in the composite system which is infinite in both the transverse and axial directions (or n and x directions, respectively). The fibers are represented by one dimensional axial springs with stiffness, $E_f A_f/\Delta x$, where $A_f = Dt$, and the matrix

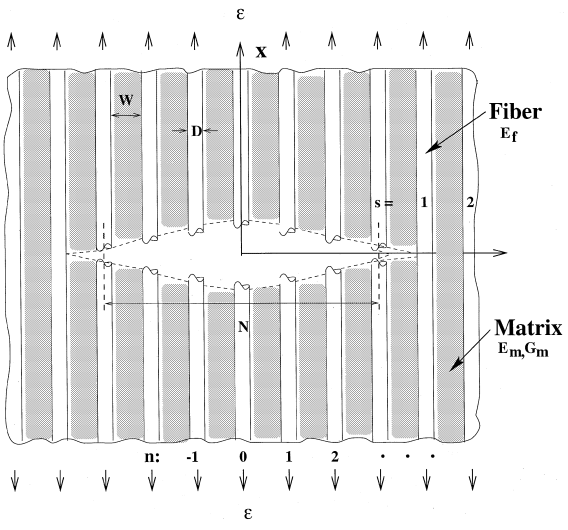

Fig. 1. The 2D unidirectional fiber composite model considered in this study, containing a transverse row of N contiguous fiber breaks and $M = N + 1$ broken matrix regions. In other words, the two "crack-tip" matrix regions, i.e., the two matrix regions between the end broken fibers and first intact fibers, are broken, which corresponds to the case (ii) examined in Section 5.

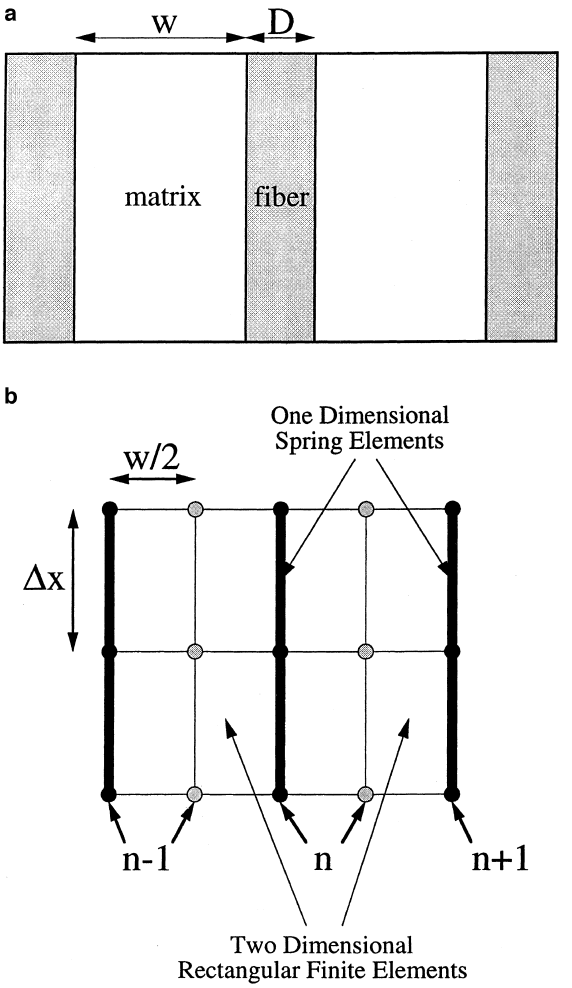

Fig. 2. The representative finite element mesh modeling the 2D fiber composite.

region between any two consecutive fiber elements is represented by a pair of rectangular finite elements. Since the transverse displacements are neglected, each element has four degrees of freedom. Fig. 3 shows the numbering scheme for the model, wherein fiber node n,i and matrix node n,i are representative nodes for all of the fiber and matrix nodes, respectively. The integer n ranges from $-\infty$ to ∞, and matrix node n is to the right of fiber n.

The governing finite element equations for fiber and matrix node n in Fig. 2 are the same as those for all other similar nodes. For fiber node n,i, the governing equation is

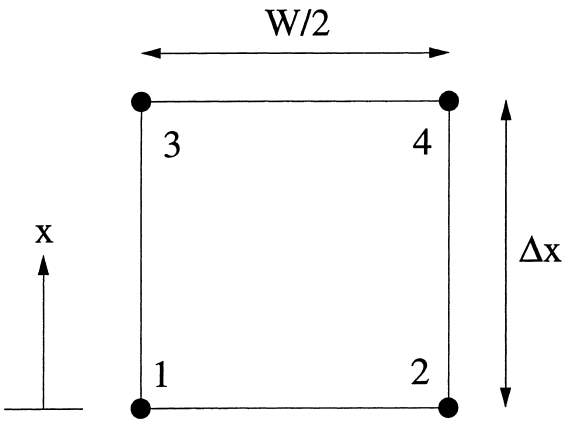

Fig. 3. The numbering scheme used to determine stiffness matrix K_{pq} for a matrix material element.

$$\left[K_{11}+K_{22}+K_{33}+K_{44}+2\frac{E_fA_f}{\Delta x}\right]U^f_{n,i} + \left[K_{13}+K_{24}-\frac{E_fA_f}{\Delta x}\right]\left(U^f_{n,i+1}+U^f_{n,i-1}\right) + [K_{12}+K_{34}]\left(U^m_{n,i}+U^m_{n-1,i}\right) + K_{14}\left(U^m_{n,i+1}+U^m_{n,i-1}+U^m_{n-1,i+1}+U^m_{n-1,i-1}\right) = 0 \quad (1a)$$

and for matrix node n,i, the governing equation is

$$[K_{11}+K_{22}+K_{33}+K_{44}]U^m_{n,i} + [K_{13}+K_{24}]\left(U^m_{n,i+1}+U^m_{n,i-1}\right) + [K_{12}+K_{34}]\left(U^f_{n,i}+U^f_{n+1,i}\right) + K_{14}\left(U^f_{n,i+1}+U^f_{n,i-1}+U^f_{n+1,i+1}+U^f_{n+1,i-1}\right) = 0, \quad (1b)$$

where U is the axial displacement of a fiber node (with superscript f) or matrix node (with superscript m) at the location denoted by the subscript. The K_{pq}'s, $p,q=1,\ldots,4$, are the stiffness values for the matrix element as determined using the principle of virtual work and the finite element method (e.g., Cook et al., 1974). Fig. 3 shows the numbering scheme for the matrix element. The stiffness term K_{pq} represents the force on matrix node p when matrix node q is given a unit displacement and all other nodes have zero displacement. These stiffness values are

$$K_{11}=K_{22}=K_{33}=K_{44}=\frac{1}{6}\frac{E_mWt}{\Delta x}+\frac{2}{3}\frac{G_mt\Delta x}{W}, \quad (2a)$$

$$K_{12}=K_{34}=\frac{1}{12}\frac{E_mWt}{\Delta x}-\frac{2}{3}\frac{G_mt\Delta x}{W}, \quad (2b)$$

$$K_{13}=K_{24}=-\frac{1}{6}\frac{E_mWt}{\Delta x}+\frac{1}{3}\frac{G_mt\Delta x}{W}, \quad (2c)$$

$$K_{14}=K_{23}=-\frac{1}{12}\frac{E_mWt}{\Delta x}-\frac{1}{3}\frac{G_mt\Delta x}{W}. \quad (2d)$$

Dividing Eqs. (1a) and (1b) by Δx and using the following two difference identities as Δx goes to zero,

$$\frac{d^2U_n}{dx^2}=\frac{U_{n,i+1}-2U_{n,i}+U_{n,i-1}}{\Delta x^2}, \quad (3a)$$

$$U_n=\frac{1}{3}(U_{n,i+1}+U_{n,i}+U_{n,i-1}), \quad (3b)$$

the model is made continuous in the x direction. This procedure transforms the set of algebraic finite element equations, Eqs. (1a) and (1b), into a set of coupled ordinary differential equations governing the axial displacements of the fibers and matrix, which become

$$\left[1+\frac{1}{3}\frac{E_mA_m}{E_fA_f}\right]\frac{d^2U^f_n}{dx^2}+\frac{1}{12}\frac{E_mA_m}{E_fA_f}\left(\frac{d^2U^m_n}{dx^2}+\frac{d^2U^m_{n-1}}{dx^2}\right)+2\frac{G_m}{E_f}\frac{t}{WA_f}\left(U^m_n+U^m_{n-1}-2U^f_n\right)=0 \quad (4a)$$

for fiber node n and

$$\frac{1}{3}\frac{E_mA_m}{E_fA_f}\frac{d^2U^m_n}{dx^2}+\frac{1}{12}\frac{E_mA_m}{E_fA_f}\left(\frac{d^2U^f_n}{dx^2}+\frac{d^2U^f_{n+1}}{dx^2}\right)+2\frac{G_m}{E_f}\frac{t}{WA_f}\left(U^f_n+U^f_{n+1}-2U^m_n\right)=0 \quad (4b)$$

for matrix node n. In Eqs. (4a) and (4b) A_m, the cross-sectional area of the matrix between two consecutive fibers, has replaced the product Wt. In a manner analogous to Hedgepeth (1961), nondimensional lengths ξ, displacements u, and stresses σ (or strains ε) are defined as

$$\xi = \sqrt{\frac{G_m}{E_f}}\sqrt{\frac{t}{W}}\frac{x}{\sqrt{A_f}}, \tag{5}$$

$$u_n^* = \sqrt{\frac{G_m}{E_f}}\sqrt{\frac{t}{W}}\frac{1}{\varepsilon}\frac{U_n^*}{\sqrt{A_f}}, \tag{6a}$$

$$\frac{\sigma_n^*}{E_*\varepsilon} = \frac{\varepsilon_n^*}{\varepsilon} = \frac{du_n^*}{d\xi}, \tag{6b}$$

attaching for $*$ the appropriate superscripts f or m to u and σ and corresponding subscript f or m to E. We also introduce a dimensionless ratio, ρ, which is the ratio of the axial stiffness of the matrix to the axial stiffness of the fiber, i.e.,

$$\rho = \frac{E_m A_m}{E_f A_f}. \tag{7}$$

With these normalizations, the governing equations become

$$\left[1+\frac{1}{3}\rho\right]\frac{d^2u_n^f}{d\xi^2} + \frac{1}{12}\rho\left(\frac{d^2u_n^m}{d\xi^2} + \frac{d^2u_{n-1}^m}{d\xi^2}\right) + 2\left(u_n^m + u_{n-1}^m - 2u_n^f\right) = 0, \tag{8a}$$

$$\frac{1}{3}\rho\frac{d^2u_n^m}{d\xi^2} + \frac{1}{12}\rho\left(\frac{d^2u_n^f}{d\xi^2} + \frac{d^2u_{n+1}^f}{d\xi^2}\right) + 2\left(u_n^f + u_{n+1}^f - 2u_n^m\right) = 0. \tag{8b}$$

Notably in normalized form, Eqs. (8a) and (8b) only contain one material system parameter, ρ.

As in all shear-lag analyses, this model provides the average axial stress over the fiber cross-section and average shear stress between adjacent fiber and matrix nodes. The shear strain, $\gamma_{n,n}$, and stress, $\tau_{n,n}$, in the left half of any matrix region n is

$$\gamma_{n,n} = \frac{2\left[U_n^m - U_n^f\right]}{W}, \tag{9a}$$

$$\tau_{n,n} = G_m\gamma_{n,n} \tag{9b}$$

and the shear strain, $\gamma_{n,n+1}$, and stress, $\tau_{n,n+1}$, in the right half of matrix region n is

$$\gamma_{n,n+1} = \frac{2[U_{n+1}^f - U_n^m]}{W}, \tag{9c}$$

$$\tau_{n,n+1} = G_m\gamma_{n,n+1}. \tag{9d}$$

However, when $\rho = 0$, the average shear strain $\gamma_n(x)$ and stress $\tau_n(x)$ between two adjacent fiber nodes are

$$\gamma_n = \frac{\left[U_{n+1}^f - U_n^f\right]}{W}, \tag{9e}$$

$$\tau_n = G_m\gamma_n. \tag{9f}$$

The non-dimensional forms for the shear strains and stresses, Eqs. (9a)–(9f), are

$$\hat{\gamma} = \frac{1}{2}\sqrt{\frac{G_m}{E_f}}\sqrt{\frac{Wt}{A_f}}\frac{\gamma}{\varepsilon}, \tag{10a}$$

$$\hat{\tau} = \frac{1}{2}\sqrt{\frac{G_m}{E_f}}\sqrt{\frac{Wt}{A_f}}\frac{\tau}{G_m\varepsilon}, \tag{10b}$$

which result in the following relationships between the normalized matrix shear strains, shear stresses, and fiber and matrix displacements:

$$\hat{\gamma}_{n,n} = \hat{\tau}_{n,n} = u_n^m - u_n^f, \tag{11a}$$

$$\hat{\gamma}_{n,n+1} = \hat{\tau}_{n,n+1} = u_{n+1}^f - u_n^m, \tag{11b}$$

when $\rho \neq 0$ and

$$\hat{\gamma}_n = \hat{\tau}_n = \frac{1}{2}\left(u_{n+1}^f - u_n^f\right), \tag{11c}$$

when $\rho = 0$.

3. Single break solutions

In this influence superposition technique, there are two separate unit solutions, which can be obtained by solving Eqs. (8a) and (8b) with the appropriate boundary conditions. The first one is the displacement and stress redistribution due to a single fiber break at fiber $n = 0$ and $\xi = 0$, and the other is the displacement and stress redistribution due to a broken matrix region at $n = 0$ at $\xi = 0$. Both problems are solved first by assuming a unit displacement is applied to each side of the (matrix or fiber) break in opposite directions, and the applied strain at infinity, ε, in both the fiber and matrix is zero. Once these two non-trivial problems are solved, a uniform strain ε is superimposed to obtain the final solution, with far field strain ε and traction-free breaks. To distinguish between these two solutions, termed 'auxiliary' solutions,

from the final solution under a uniform far field strain (and no axial stress at the breaks), the symbols v_n^{f} and v_n^{m} are used for the normalized fiber and matrix displacements, respectively, in the single fiber break problem, and w_n^{f} and w_n^{m} are used in the single broken matrix problem. The symbols u_n^{f} and u_n^{m} are reserved for the final solution developed in Section 4. Accordingly, Eqs. (8a) and (8b) become the governing set of equations for the displacements in the first auxiliary problem by replacing u_n^{f} and u_n^{m} by v_n^{f} and v_n^{m}. For the first problem of a single break in fiber $n=0$ at $\xi=0$, the boundary conditions are

$$v_n^{\mathrm{f}}(0)=1 \quad \text{for } n=0, \tag{12a}$$

$$v_n^{\mathrm{f}}(0)=0 \quad \text{for } n\neq 0, \tag{12b}$$

$$v_n^{\mathrm{m}}(0)=0 \quad \text{for all } n, \tag{12c}$$

$$\frac{\mathrm{d}v_n^{\mathrm{f,m}}}{\mathrm{d}\xi}(\infty)=0 \quad \text{for all } n \tag{12d}$$

for $\rho>0$ and $\xi\geqslant 0$. The system of equations for the second problem of a matrix break are the same as Eqs. (8a) and (8b) but with w_n^{f} and w_n^{m} in place of u_n^{f} and u_n^{m}. The boundary conditions for this problem are

$$w_n^{\mathrm{f}}(0)=0 \quad \text{for all } n, \tag{13a}$$

$$w_n^{\mathrm{m}}(0)=1 \quad \text{for } n=0, \tag{13b}$$

$$w_n^{\mathrm{m}}(0)=0 \quad \text{for } n\neq 0, \tag{13c}$$

$$\frac{\mathrm{d}w_n^{\mathrm{f,m}}}{\mathrm{d}\xi}(\infty)=0 \quad \text{for all } n \tag{13d}$$

for $\rho>0$ and $\xi\geqslant 0$. The method of solution is the same for both problems and thus, is described in detail for the single fiber break problem only, Eqs. (12a)–(12d).

To obtain the solution to the fiber break problem for v_n^{f} and v_n^{m}, the first step is to apply the following discrete Fourier transform to Eqs. (8a) and (8b),

$$\bar{v}^*(\xi,\theta)=\sum_{n=-\infty}^{\infty} v_n^* \mathrm{e}^{-\mathrm{i}n\theta}, \tag{14}$$

attaching for $*$ appropriate superscripts f or m depending on the case. Later, the associated inverse transform will be applied to regain dependence on n,

$$v_n^*(\xi)=\frac{1}{2\pi}\int_{-\pi}^{\pi}\bar{v}^*(\xi,\theta)\mathrm{e}^{\mathrm{i}n\theta}\,\mathrm{d}\theta. \tag{15}$$

Applying Eq. (14) to Eqs. (8a) and (8b) and adding the equations together yields two coupled governing equations for the transformed variables $\bar{v}^{\mathrm{f}}$ and $\bar{v}^{\mathrm{m}}$,

$$\left(1+\frac{1}{3}\rho\right)\frac{\partial^2\bar{v}^{\mathrm{f}}}{\partial\xi^2}+\frac{1}{12}\alpha\rho\frac{\partial^2\bar{v}^{\mathrm{m}}}{\partial\xi^2}+2\alpha\bar{v}^{\mathrm{m}}-4\bar{v}^{\mathrm{f}}=0, \tag{16a}$$

$$\frac{1}{3}\rho\frac{\partial^2\bar{v}^{\mathrm{m}}}{\partial\xi^2}+\frac{1}{12}\beta\rho\frac{\partial^2\bar{v}^{\mathrm{f}}}{\partial\xi^2}+2\beta\bar{v}^{\mathrm{f}}-4\bar{v}^{\mathrm{m}}=0, \tag{16b}$$

where $\alpha=1+e^{-\mathrm{i}\theta}$ and $\beta=1+e^{\mathrm{i}\theta}$. The boundary conditions, Eqs. (12a)–(12d), transform to

$$\bar{v}^{\mathrm{f}}(0,\theta)=1, \tag{17a}$$

$$\bar{v}^{\mathrm{m}}(0,\theta)=0, \tag{17b}$$

$$\frac{\partial\bar{v}^{\mathrm{f}}}{\partial\xi}(\infty,\theta)=0, \tag{17c}$$

$$\frac{\partial\bar{v}^{\mathrm{m}}}{\partial\xi}(\infty,\theta)=0. \tag{17d}$$

Eqs. (16a) and (16b) represent a system of coupled ordinary differential equations, whose solution can be obtained using well-known procedures (e.g., See Nagle and Saff, 1986). Applying boundary conditions (17), the transformed solution for $\xi\geqslant 0$ is

$$\bar{v}^{\mathrm{f}}(\xi,\theta)=\frac{1}{2\chi}\{(\chi-1)\exp[-\eta\lambda_1\xi]+(\chi+1)\exp[-\eta\lambda_2\xi]\}, \tag{18a}$$

$$\bar{v}^{\mathrm{m}}(\xi,\theta)=\frac{-(\chi^2-1)}{\chi\alpha\rho}\{\exp[-\eta\lambda_1\xi]-\exp[-\eta\lambda_2\xi]\}, \tag{18b}$$

where

$$\lambda_1^2=\frac{\rho}{3}\left[2+\cos^2(\theta/2)\right]+1+\chi, \tag{19a}$$

$$\lambda_2^2=\frac{\rho}{3}\left[2+\cos^2(\theta/2)\right]+1-\chi, \tag{19b}$$

$$\chi=\sqrt{\rho^2\cos^2(\theta/2)+2\rho\cos^2(\theta/2)+1}, \tag{19c}$$

$$\eta = \frac{72}{12\rho(1+\rho/3) - \rho^2\cos^2(\theta/2)} \tag{19d}$$

for $\rho > 0$. To re-gain dependence on n, the inverse transform Eq. (15) is applied to Eqs. (18a) and (18b). Then the solution for the full plane, $-\infty < \xi < \infty$, is constructed by noting that the displacements are antisymmetric about $\xi = 0$. Therefore, for $-\infty < \xi < \infty$, ξ is replaced with $|\xi|$, and the function $\mathrm{sgn}(\xi)$ is used to account for the asymmetry in the displacements. The normalized fiber and matrix displacements due to a single broken fiber are

$$v_n^{\mathrm{f}}(\xi) = \frac{\mathrm{sgn}(\xi)}{2\pi}\int_0^{\pi} \frac{\cos(n\theta)}{\chi}\{(\chi-1)\exp[-\eta\lambda_1|\xi|] + (\chi+1)\exp[-\eta\lambda_2|\xi|]\}\,\mathrm{d}\theta, \tag{20}$$

$$v_n^{\mathrm{m}}(\xi) = -\frac{\mathrm{sgn}(\xi)(\rho+2)}{4\pi} \times \int_0^{\pi} \frac{\cos(n\theta)+\cos[(n+1)\theta]}{\chi} \times \{\exp[-\eta\lambda_1|\xi|] - \exp[-\eta\lambda_2|\xi|]\}\,\mathrm{d}\theta, \tag{21}$$

where $\mathrm{sgn}(\xi) = 1$ when $\xi \geqslant 0^+$ and $\mathrm{sgn}(\xi) = -1$ when $\xi \leqslant 0^-$. Note that γ, λ_1, λ_2, and χ are all positive, and since these are also even functions in θ, the imaginary part introduced by the inverse transform is zero. The normalized fiber and matrix stresses $p_n^{\mathrm{f,m}}(\xi)$ for the single fiber break problem are

$$p_n^{\mathrm{f}}(\xi) = -\frac{1}{2\pi}\int_0^{\pi} \frac{\eta\cos(n\theta)}{\chi}\{\lambda_1(\chi-1)\exp[-\eta\lambda_1|\xi|] + \lambda_2(\chi-1)\exp[-\eta\lambda_2|\xi|]\}\,\mathrm{d}\theta, \tag{22}$$

$$p_n^{\mathrm{m}}(\xi) = \frac{\rho+2}{4\pi}\int_0^{\pi} \frac{\eta\{\cos(n\theta)+\cos[(n+1)\theta]\}}{\chi} \times \{\lambda_1\exp[-\eta\lambda_1|\xi|] - \lambda_2\exp[-\eta\lambda_2|\xi|]\}\,\mathrm{d}\theta. \tag{23}$$

Returning now to the second problem of a single broken matrix node, the resulting normalized fiber and matrix tensile displacements $w_n^{\mathrm{f,m}}(\xi)$ and stresses $q_n^{\mathrm{f,m}}(\xi)$ are

$$w_n^{\mathrm{f}}(\xi) = -\frac{\mathrm{sgn}(\xi)\rho}{4\pi}\int_0^{\pi} \frac{\cos(n\theta)+\cos[(n-1)\theta]}{\chi} \times \{\exp[-\eta\lambda_1|\xi|] - \exp[-\eta\lambda_2|\xi|]\}\,\mathrm{d}\theta, \tag{24}$$

$$w_n^{\mathrm{m}}(\xi) = \frac{\mathrm{sgn}(\xi)}{2\pi}\int_0^{\pi} \frac{\cos(n\theta)}{\chi}\{(\chi+1)\exp[-\eta\lambda_1|\xi|] + (\chi-1)\exp[-\eta\lambda_2|\xi|]\}\,\mathrm{d}\theta, \tag{25}$$

$$q_n^{\mathrm{f}}(\xi) = \frac{\rho}{4\pi}\int_0^{\pi} \frac{\eta\{\cos(n\theta)+\cos[(n-1)\theta]\}}{\chi} \times \{\lambda_1\exp[-\eta\lambda_1|\xi|] - \lambda_2\exp[-\eta\lambda_2|\xi|]\}\,\mathrm{d}\theta, \tag{26}$$

$$q_n^{\mathrm{m}}(\xi) = -\frac{1}{2\pi}\int_0^{\pi} \frac{\eta\cos(n\theta)}{\chi}\{\lambda_1(\chi+1)\exp[-\eta\lambda_1|\xi|] + \lambda_2(\chi-1)\exp[-\eta\lambda_2|\xi|]\}\,\mathrm{d}\theta, \tag{27}$$

for $\rho > 0$. As before where η, λ_1, λ_2, and χ are defined in Eqs. (16a) and (16b).

Since these solutions are translation invariant, the solution for an arbitrarily located fiber break at (n_j, ξ_j) or matrix break at (n_k, ξ_k) is obtained by simply shifting n and ξ in Eqs. (20)–(23) by $-n_j$ and $-\xi_j$, respectively, or n and ξ in Eqs. (24)–(27) by $-n_k$ and $-\xi_k$. These shifted solutions will be used frequently in Section 4 describing the stress analysis for multiple fiber and matrix breaks in any given configuration.

4. Influence superposition technique for multiple breaks

In this section, we describe how these two elastic shear-lag solutions, derived in Section 3, one due to a single fiber break and the other due to a single matrix break, are used to calculate the fiber and matrix axial stresses and strains and matrix shear stresses given ρ due to any number and arbitrary arrangement of broken fibers and matrix regions. Boundary conditions for this general

problem of multiple break sites are zero stress at all broken sites and a far field strain ε.

Suppose there are N fiber breaks, where the jth fiber break is located on a fiber at (n_j, ξ_j), $j = 1, \ldots, N$, and there are M matrix breaks where the kth matrix break is centered in a matrix region at (n_k, ξ_k), $k = 1, \ldots, M$. The stress at any fiber position (n, ξ), is

$$\frac{\sigma_n^{\mathrm{f}}(\xi)}{E_{\mathrm{f}}\varepsilon} = \frac{\varepsilon_n^{\mathrm{f}}(\xi)}{\varepsilon} = 1 + \frac{1}{2}\sum_{j=1}^{N} \omega_j^{\mathrm{f}} p_{n-n_j}^{\mathrm{f}}(\xi - \xi_j) + \frac{1}{2}\sum_{j=1}^{\mathrm{m}} \omega_j^{\mathrm{m}} q_{n-n_k}^{\mathrm{f}}(\xi - \xi_k), \tag{28}$$

where the ω^{f}'s are weighting factors for fiber breaks and ω^{m}'s are the weighting factors for matrix breaks. Similarly, the axial stress along the center of a matrix region (n,ξ), is

$$\frac{\sigma_n^{\mathrm{m}}(\xi)}{E_{\mathrm{m}}\varepsilon} = \frac{\varepsilon_n^{\mathrm{m}}(\xi)}{\varepsilon} = 1 + \frac{1}{2}\sum_{j=1}^{N} \omega_j^{\mathrm{f}} p_{n-n_j}^{\mathrm{m}}(\xi - \xi_j) + \frac{1}{2}\sum_{j=1}^{\mathrm{M}} \omega_j^{\mathrm{m}} q_{n-n_k}^{\mathrm{m}}(\xi - \xi_k). \tag{29}$$

Physically, the weighting factor, say ω_j^{f} for fiber break j, is the crack opening displacement of fiber break j. The N unknown ω_j^{f}'s and M unknown ω_k^{m}'s are determined from the knowledge that the axial stress at each break site is zero, i.e.,

$$\frac{\sigma_{n_j}^{\mathrm{f}}}{E_{\mathrm{f}}\varepsilon}(\xi_j) = 0 \quad \text{for} \quad j = 1, \ldots, N, \qquad \frac{\sigma_{n_k}^{\mathrm{m}}}{E_{\mathrm{m}}\varepsilon}(\xi_k) = 0 \quad \text{for} \quad k = 1, \ldots, M. \tag{30}$$

Combining Eqs. (28)–(30) leads to $N + M$ equations for the $N + M$ weighting factors.

The first step is to determine from the two single break solutions, $p_n^{\mathrm{f}}(\xi)$, $q_n^{\mathrm{f}}(\xi)$, $p_n^{\mathrm{m}}(\xi)$, and $q_n^{\mathrm{m}}(\xi)$, the axial stresses transmitted between all pairs of fiber and matrix breaks. Accordingly, these *influence functions* will depend on the distance between the relevant fiber or matrix breaks. From the single fiber break problem, the influence function, Λ_{ij}, is defined as the normalized axial stress transmitted onto fiber break i at (n_i, ξ_i) due to a unit opening displacement of fiber break j at (n_j, ξ_j). Specifically, using Eq. (22), Λ_{ij} is

$$\Lambda_{ij} = \frac{1}{2} p_{n_i - n_j}^{\mathrm{f}}(\xi_i - \xi_j). \tag{31}$$

Note that $\Lambda_{ji} = \Lambda_{ij}$. Similarly, Ω_{kj} is defined as the normalized axial stress transmitted onto matrix region k at (n_k, ξ_k) due to a unit opening displacement of fiber break j at (n_j, ξ_j). Using Eq. (23), Ω_{kj} is

$$\Omega_{kj} = \frac{1}{2} p_{n_k - n_j}^{\mathrm{m}}(\xi_k - \xi_j). \tag{32}$$

Turning now to the single matrix break problem, Φ_{il} is defined as the normalized axial stress transmitted onto fiber break i at (n_i, ξ_i) due a unit opening displacement at matrix break l at (n_l, ξ_l). Using Eq. (26), Φ_{il} is

$$\Phi = \frac{1}{2} q_{n_i - nl}^{\mathrm{f}}(\xi_i - \xi_l). \tag{33}$$

Lastly, Ψ_{kl} is defined as the normalized axial stress transmitted to matrix break k at (n_k, ξ_k) due to a unit opening displacement of matrix break l at (n_l, ξ_l). Specifically, using Eq. (27), Ψ_{kl} is

$$\Psi_{kl} = \frac{1}{2} q_{n_k - nl}^{\mathrm{m}}(\xi_k - \xi_l). \tag{34}$$

Once the influence functions are determined for a given set of broken fiber and matrix sites, the next step is to solve for the proper weighting factors ω_j^{f} corresponding to the fiber breaks and ω_k^{m} corresponding to the matrix breaks, such that there exists zero stress at all broken sites (i.e., Eq. (30)). So for N fiber breaks and M matrix breaks, the following system of $N + M$ equations is solved for the $N\omega_j^{\mathrm{f}}$'s and $M\omega_k^{\mathrm{m}}$'s,

$$\begin{bmatrix} \Lambda & \Phi \\ \Omega & \Psi \end{bmatrix} \begin{Bmatrix} \omega^{\mathrm{f}} \\ \omega^{\mathrm{m}} \end{Bmatrix} = \begin{Bmatrix} -1 \\ -1 \end{Bmatrix}. \tag{35}$$

In this $N + M$ system of equations, ω^{f} is an N-dimensional vector, ω^{m} is an M-dimensional vector, and Λ , Ω, Φ, and Ψ have dimensions $N \times N$, $M \times N$, $N \times M$, and $M \times M$, respectively. The matrices Λ and Ψ are symmetric. The $N + M$ dimensional vector on the right-hand side of Eq. (35) is simply a vector filled with -1's. Also

the square matrix in Eq. (35) is negative definite. The proof of this fact is similar to proving that a finite element stiffness matrix is positive definite.

Here we point out one of the main advantages of this technique: the computation time involves solving for the weighting factors in Eq. (35), which only depends on the number of damaged elements in the lamina, and calculating the fiber and matrix and displacements using Eqs. (28), (29), (36) and (37). In the present work, these weighting factors are determined by Gaussian elimination. However, if this method is used to study failure progression (i.e., accumulation of damage with increasing applied strain), Eq. (35) needs to be solved repeatedly and is suited for an inversion by matrix partitioning scheme (Press et al., 1992).

With the weighting factors ω^{f} and ω^{m} solved for in Eq. (35), the fiber and matrix axial stresses for any n and at any axial distance ξ are simply calculated using Eqs. (28) and (29). Similarly, the normalized fiber and matrix displacements, $u_n^{\mathrm{f}}(\xi)$ and $u_n^{\mathrm{m}}(\xi)$, are

$$u_n^{\mathrm{f}}(\xi) = \xi + \frac{1}{2}\sum_{j=1}^{N}\omega_j^{\mathrm{f}} v_{n-n_j}^{\mathrm{f}}(\xi-\xi_j) + \frac{1}{2}\sum_{k=1}^{\mathrm{M}}\omega_k^{\mathrm{m}} w_{n-n_j}^{\mathrm{f}}(\xi-\xi_k), \tag{36}$$

$$u_n^{\mathrm{m}}(\xi) = \xi + \frac{1}{2}\sum_{j=1}^{N}\omega_j^{\mathrm{f}} v_{n-n_j}^{\mathrm{m}}(\xi-\xi_j) + \frac{1}{2}\sum_{k=1}^{\mathrm{M}}\omega_k^{\mathrm{m}} w_{n-n_j}^{\mathrm{m}}(\xi-\xi_k). \tag{37}$$

Lastly, the normalized matrix shear stresses and strains can be calculated by substituting Eqs. (36) and (37) into Eqs. (11a)–(11c).

Since the aforementioned influence functions for axial stresses and displacements are a function only of the relative break locations, $|n_i - n_j|$ and $|\xi_i - \xi_j|$, they can be integrated numerically between the desired values of $|n_i - n_j|$ and $|\xi_i - \xi_j|$ and stored prior to performing calculations. Later, when the break positions are specified, these values for the influence functions are accessed using an interpolation routine when calculating for the weighting factors in Eq. (35) and the resulting stress and displacement fields, Eqs. (28), (29), (36) and (37). Specifically, the influence functions are evaluated numerically using a fourth-order Runge–Kutta routine (Press et al., 1992).

For illustration, this technique is used to examine various cases involving a 'crack' or cluster of broken fibers and matrix, transversely aligned along the $\xi = 0$ plane as shown in Fig. 1. On the right side of the crack in Fig. 1, the intact fibers starting from the first surviving fiber ahead of the last broken one (fiber $n = (N-1)/2$) are numbered $s = 1, \ldots, \infty$. For a crack containing N fiber breaks, all fibers in the range $-(N-1)/2 \leqslant n \leqslant (N-1)/2$ are broken. For instance, when $N = 301$, fibers $n = -150$ through $n = 150$ are broken, and when $N = 1$, we have a single break, and only fiber $n = 0$ is broken. In most of the examples, two subcases are examined: case (i) only the matrix regions between two broken fibers are broken and case (ii) in addition to those broken in case (i), the two "crack-tip" matrix regions between the last broken fiber and first intact fiber are broken as well. (Case (ii) is illustrated in Fig. 1). Therefore when $N = 301$, $M = 300$, and matrix regions $n = -150$ through $n = 149$ are broken in case (i), and $M = 302$, and matrix regions $n = -151$ through $n = 150$ are broken in case (ii). Likewise, when $N = 1$, $M = 0$ in case (i) and $M = 2$, where matrix regions $n = -1$ and 0 are broken in case (ii). The Hedgepeth model, which corresponds to the $\rho = 0$ results in the present model, does not differentiate between broken or unbroken crack-tip matrix regions.

These special cases ranging from a single break to large central cracks are considered for the insight they give and for comparison with other theoretical work (thus far restricted to such idealized configurations) and in-plane 2D linear elasticity. However, in using this technique, computation time would be the same if these breaks were spatially dispersed in any arbitrary arrangement. Such cases will naturally be considered when incorporating this technique in failure simulations and crack-tip studies in composites. Subsequent computations for results to follow take from less than a few minutes to at most half an hour on a workstation (e.g., Silicon Graphics, Inc. O2™).

5. Results

Results, as predicted by this shear-lag model, are presented, for the fiber and matrix stresses around a single break and cracks from cases (i) and (ii) described previously. Though ρ can range from 0 to ∞, we focus our investigation on the more practical range of $0 \leqslant \rho \leqslant 2$. Low values of ρ best represent high V_f PMCs (e.g., $\rho = 0.01$, when $E_m/E_f = 1/100$ and $A_m/A_f = 1$); whereas high values of ρ represent low V_f CMCs (e.g., $\rho = 2.00$, when $E_m/E_f = 1/2$ and $A_m/A_f = 4$). Cracks are represented by a transverse row of contiguous fiber and matrix breaks, wherein the number of fiber breaks ranges from $N = 1$ to $N = 301$ (see Fig. 1).

5.1. Crack-tip stress concentrations

In this section, we focus on two parameters, which are often used to quantify stress transfer; the crack-tip stress concentrations and overstress transfer length, x_c, (or ξ_c in normalized form). The latter is defined as the axial distance from $\xi = 0$ to where the local fiber stress is greater than the far field stress along the first broken fiber ($s = 1$).

Axial stress concentrations in the fiber and matrix, $\sigma_n^f(\xi)/E_f\varepsilon$ and $\sigma_n^m(\xi)/E_m\varepsilon$, computed directly from Eqs. (28) and (29) are normalized by the far field stress in their respective phase. To normalize both the local fiber and matrix axial stresses by the composite far field stress, $E\varepsilon$, the following relationships are used,

$$\frac{V_f\sigma_n^f(\xi)}{E\varepsilon} = \frac{1}{\rho+1}\,\frac{\sigma_n^f(\xi)}{E_f\varepsilon}, \tag{38}$$

$$\frac{(1-V_f)\sigma_n^m(\xi)}{E\varepsilon} = \frac{\rho}{\rho+1}\,\frac{\sigma_n^m(\xi)}{E_m\varepsilon} \tag{39}$$

for $\rho \geqslant 0$. In Eqs. (38) and (39), E is the overall composite axial stiffness defined by the rule of mixtures, i.e., $E = V_fE_f + (1 - V_f)E_m$. When $\rho = 0$, only the fibers sustain axial stress, and the results reduce to those of Hedgepeth's 2D shear-lag model (1961).

Table 1 shows the values for the axial stresses normalized by the composite far field stress, Eqs. (38) and (39), in the first surviving fiber ($s = 1$) adjacent to a row of N breaks for different N and ρ in the range 0–2. In calculating values listed in Table 1, the crack-tip matrix regions are intact and so $M = N - 1$. As shown, the fiber stress decreases and the matrix stress increases as ρ increases for all N. Also, as N increases, the rate of change of the stress concentrations to increases in ρ also increases, but at a decaying rate. Furthermore, results in Table 1 shows that as both N and ρ increase, it is possible for $(1 - V_f)\sigma^m > V_f\sigma^f$.

Values shown in Table 1 are calculated assuming that the matrix regions between the last broken and first intact fiber at both ends are intact (i.e., case (i)). Clearly as ρ increases and the stress concentrations in this matrix region increase, it becomes likely that this matrix region could break, especially if its failure strain is comparable to that of the fiber. Results from this shear-lag model show significant differences in stress redistribution when these "crack-tip" matrix regions are broken (e.g. see Fig. 1) versus when they are fully intact. This is shown in Fig. 4 which plots the fiber stress concentration at $\xi = 0$ on the first intact fiber ahead of $N = 1$ or 2 fiber breaks versus ρ for case (i) and (ii). As seen in Fig. 4, when the crack-tip matrix regions are intact, case (i), the stress concentration $\sigma_n^f(0)/E_f\varepsilon$ in the first intact fiber monotonically decreases with ρ. When they are broken, case (ii), this stress increases with ρ due to the additional load transferred from the broken matrix. However as ρ increases, the portion of the total applied stress $E\varepsilon$ sustained by the fibers decreases, and thus, the fiber stress, $V_f\sigma_n^f(0)/E\varepsilon$, decreases with ρ, in both cases (i) and (ii) for all N. Also $V_f\sigma_n^f(0)/E\varepsilon$ remains higher in magnitude in case (ii), than that in the intact matrix case (i) for all values of ρ and N.

5.2. Overstress transfer length

In the case of $\rho = 0$, the overstress length x_c depends on the square root of the fiber axial and matrix shear modulus ratio and the fiber volume fraction and in normalized form ξ_c, (5), is $\sim$1.05 for a single break. However when $E_m \neq 0$, ξ_c may grow much longer. This behavior is demonstrated in Fig. 4 which also shows the increases in ξ_c with increases in ρ when $N = 1$ and the crack-tip matrix regions are intact (solid triangles). When the

Table 1
Stress concentration factors (normalized by far field composite stress) in the first fiber and matrix region ahead and in-line of a row of N fiber breaks (and $M = N - 1$ matrix breaks) for various values of ρ

	ρ	$V_f\sigma_n^f(0)/E\varepsilon$	$V_m\sigma_n^m(0)/E\varepsilon$	$\varepsilon_N^H(0)/\varepsilon$, Eq. (41)
$N=1$	0.00	1.333	0.000	1.253
	0.01	1.269	0.134	
	0.05	1.090	0.291	
	0.10	1.199	0.403	
	0.50	0.741	0.786	
	1.00	0.535	0.976	
	2.00	0.349	1.141	
$N=2$	0.00	1.600	0.000	1.535
	0.01	1.510	0.201	
	0.05	1.448	0.437	
	0.10	1.274	0.601	
	0.50	0.847	1.146	
	1.00	0.610	1.406	
	2.00	0.917	1.627	
$N=21$	0.00	4.180	0.000	4.157
	0.01	3.897	0.687	
	0.05	3.510	1.486	
	0.10	3.208	2.036	
	0.50	2.069	3.811	
	1.00	1.465	4.628	
	2.00	0.929	5.311	
$N=51$	0.00	6.406	0.000	6.391
	0.01	5.965	1.074	
	0.05	5.366	2.322	
	0.10	4.902	3.181	
	0.50	3.163	5.947	
	1.00	2.230	7.218	
	2.00	1.413	8.280	
$N=101$	0.00	8.961	0.000	8.950
	0.01	8.342	1.513	
	0.05	7.501	3.272	
	0.10	6.850	4.480	
	0.50	4.401	8.706	
	1.00	3.113	10.167	
	2.00	1.970	11.653	
$N=201$	0.00	12.602	0.000	12.586
	0.01	11.728	2.135	
	0.05	10.546	4.618	
	0.10	9.627	6.322	
	0.50	6.183	11.812	
	1.00	4.374	14.338	
	2.00	2.767	16.435	
$N=301$	0.00	15.403	0.000	15.401
	0.01	12.890	2.613	
	0.05	13.535	5.652	
	0.10	11.765	7.736	

Table 1 (Continued)

ρ	$V_f\sigma_n^f(0)/E\varepsilon$	$V_m\sigma_n^m(0)/E\varepsilon$	$\varepsilon_N^H(0)/\varepsilon$, Eq. (41)
0.50	7.555	14.454	
1.00	5.344	17.547	
2.00	3.379	20.107	

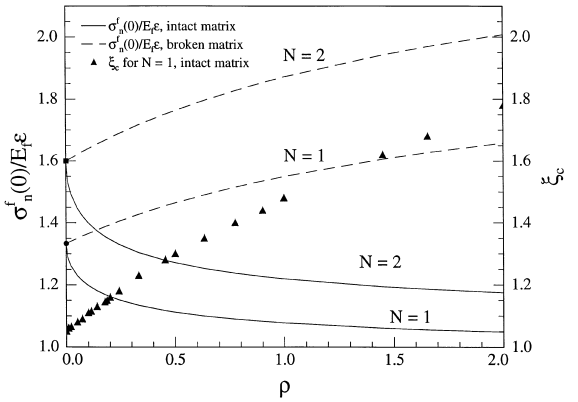

Fig. 4. The break plane ($\xi=0$) fiber stress concentration $\sigma_n^f(0)/E_f\varepsilon$ (dashed and thin solid lines) and ξ_c overstress transfer length (thick solid line) versus $\rho=E_m/E_f$ for $N=1$ and 2 breaks. The dashed and thin solid lines correspond to case (i) where crack-tip matrix regions are intact and case (ii) where the crack-tip matrix regions are broken.

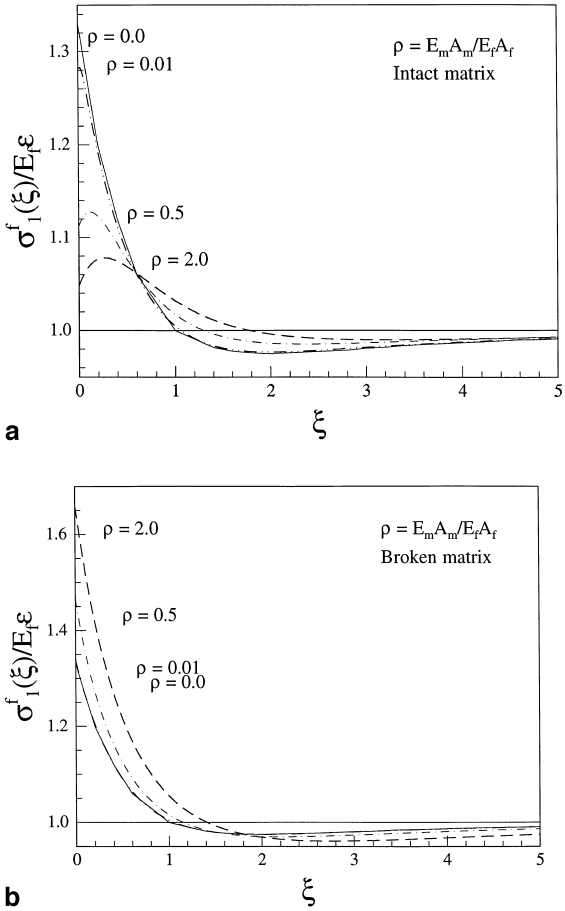

Fig. 5. The fiber axial stress profile along an intact fiber immediately adjacent to a single fiber break at $\xi=0$ for different values of ρ, when the (a) crack-tip matrix regions are intact and (b) they are broken.

crack-tip matrix regions are broken, ξ_c also increases with ρ, but at a much slower rate. For instance, for $\rho=0.1$, $\xi_c=1.11$ in case (i) and $\xi_c=1.07$ in case (ii) and for $\rho=1.0$, $\xi_c=1.48$ in case (i) and $\xi_c=1.24$ in case (ii). As in Hedgepeth's shear-lag model, the overstress region is longer in fibers farther from the break or crack-tip. Similarly, the overstress length in the matrix ξ_c^m grows with ρ and in case (i), $\xi_c^m<\xi_c$. Nevertheless, these trends in ξ_c show that although the actual fiber stress may decrease as ρ increases, the length of fiber susceptible to fracture increases. This can lead to important trade-offs with respect to the statistics of fiber strength and resulting fiber fracture pattern. Trends similar to those illustrated in Fig. 4 arise for larger N as well.

The behavior of fiber stress concentrations and ξ_c with changes in ρ can also be seen in more detail in Fig. 5. Fig. 5 shows the longitudinal axial tensile stress profiles along the first intact fiber neighboring a single fiber break with (a) intact surrounding matrix regions and (b) broken matrix regions. Another marked difference between these two cases, not noted earlier, is that in case (i) the maximum stress concentration occurs a distance away from the break plane $\xi=0$. The location of this maximum, ξ^*, moves further from the break plane as ρ increases. This rise and fall in the fiber stress profile is also seen in many FEM calculations (e.g., Nedele and Wisnom, 1994) and

in linear elasticity solutions (Sih, 1981). Many have argued that this local rise in axial stress immediately away from the crack plane is due to local bending; however, in our case, there can be no bending; only axial displacements and in-plane matrix shear are realized.

To understand this behavior in accordance with our model assumptions, we return to the governing equilibrium equations for matrix node n, Eq. (8b). Using Eqs. (6b), (11a), (11b), we rewrite Eq. (8b) to obtain the following relation between the slope of the strain concentration in fiber $n+1$ and the slope of the strain concentration in matrix n and fiber n,

$$\frac{\mathrm{d}(\sigma_{n+1}^{\mathrm{f}}/E_{\mathrm{f}}\varepsilon)}{\mathrm{d}\xi} = \frac{24}{\rho}\,(\hat{\tau}_{n,n} - \hat{\tau}_{n,n+1}) - 4\frac{\mathrm{d}(\sigma_n^{\mathrm{m}}/E_{\mathrm{m}}\varepsilon)}{\mathrm{d}\xi} - \frac{\mathrm{d}(\sigma_n^{\mathrm{f}}/E_{\mathrm{f}}\varepsilon)}{\mathrm{d}\xi}. \tag{40}$$

Therefore the rise in $\sigma_{n+1}^{\mathrm{f}}$ occurs for ξ when the right-hand side of (40) is positive. When fiber n is broken and in case (i), the first term on the right-hand side does not change sign and is negative over the length ξ^* and the difference $(\hat{\tau}_{n,n} - \hat{\tau}_{n,n+1})$ decreases as ρ decreases. Also since fiber n is broken but matrix n is intact, $\mathrm{d}\sigma_n^{\mathrm{f}}(\xi)/\mathrm{d}\xi > 0$ and $\mathrm{d}\sigma_n^{\mathrm{m}}(\xi)/\mathrm{d}\xi < 0$ for $|\xi| > 0$. Therefore, it is the second term on the right-hand side of Eq. (40) involving $\mathrm{d}\sigma_n^{\mathrm{m}}(\xi)/\mathrm{d}\xi$, which primarily contributes to the rise in $\sigma_{n+1}^{\mathrm{f}}$ for case (i). However in case (ii) when both fiber n and matrix n are broken, both $\mathrm{d}\sigma_n^{\mathrm{m}}(\xi)/\mathrm{d}\xi > 0$ and $\mathrm{d}\sigma_n^{\mathrm{f}}(\xi)/\mathrm{d}\xi > 0$, and thus according to Eq. (40), $\mathrm{d}\sigma_{n+1}^{\mathrm{f}}(\xi)/\mathrm{d}\xi < 0$ for $|\xi| > 0$. Therefore as seen in Fig. 5(b), the local rise in $\sigma_{n+1}^{\mathrm{f}}(\xi)$ does not occur.

Within one matrix region, Eqs. (11a) and (11b) give the average normalized shear stress to the left and right of matrix node n, or $\hat{\tau}_{n,n}$ and $\hat{\tau}_{n,n+1}$, respectively. Fig. 6 shows these shear stresses within the (a) intact and (b) broken neighboring matrix region adjacent to a single fiber break for $\rho = 0.01$, 0.1, and 0.5. Also shown is $\hat{\tau}_n$ (9e)–(9f), the normalized shear stress in matrix n as calculated in the Hedgepeth (1961) shear-lag model, which corresponds to $\rho = 0$ in Fig. 6. From Eqs. (8a), (8b), (9a)–(9f), (11a)–(11c), the relation between $\hat{\tau}_n$ and the present $\hat{\tau}_{n,n+1}$ and $\hat{\tau}_{n,n}$ is $\hat{\tau}_n(\xi) = \hat{\tau}_{n,n+1}(\xi) = \hat{\tau}_{n,n}(\xi)$ as $\rho \to 0$. In Fig. 6(a), the peak values at $\xi = 0$ for $\hat{\tau}_n$ ($\rho = 0$) and $\hat{\tau}_{n,n}$ for $\rho = 0.01$, 0.10, and 0.50 are 0.7386, 0.6737, and 0.6357, respectively. As shown in Fig. 6, in both cases (i) and (ii), as ρ increases or as the matrix sustains more axial tension, the differences in magnitude between $\hat{\tau}_{n,n+1}$ and $\hat{\tau}_{n,n}$ close to the break plane $\xi = 0$ grow. Also in Fig. 6, we find that the highest shear stresses are generated between a broken and intact node and increase with ρ, while those between two intact or two broken nodes are lower and decrease with ρ. For instance in case (i), $\hat{\tau}_{n,n}$, the average shear between the broken fiber and intact matrix node,

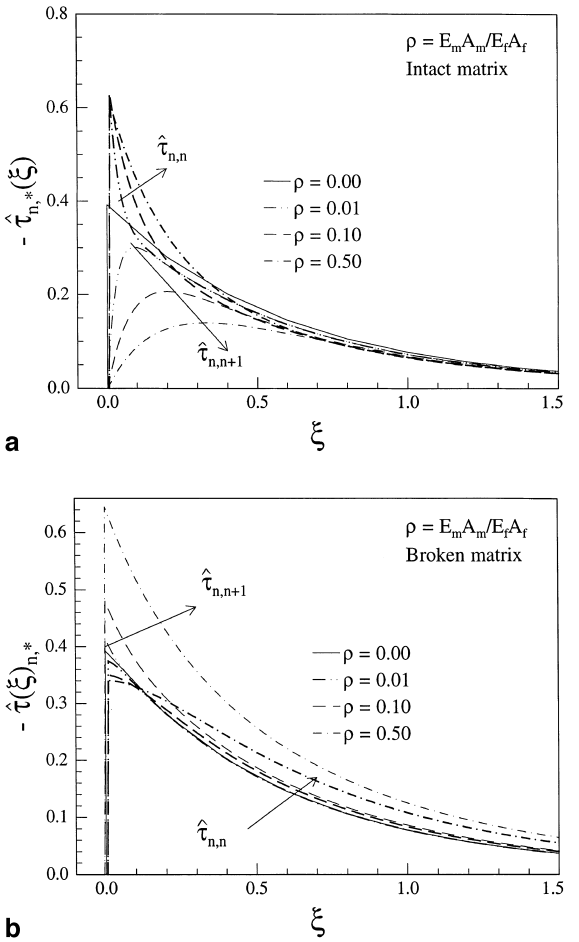

Fig. 6. The normalized matrix shear stress along the matrix region immediately adjacent to a single fiber break at $\xi = 0$ for different values of ρ, when this (a) matrix region is intact and (b) it is broken.

grows higher than $\hat{\tau}_{n,n+1}$, the average shear between two intact nodes. However in case (ii), $\hat{\tau}_{n,n}$ now between the broken matrix and fiber nodes is reduced below $\hat{\tau}_{n,n+1}$ and decreases with ρ. Also in case (ii), the maximum of $\hat{\tau}_{n,n}$ and $\hat{\tau}_{n,n+1}$ occur along the break plane $\xi = 0$, whereas in case (i), $\hat{\tau}_{n,n+1} = 0$ at $\xi = 0$, and achieves a maximum at an axial distance away from the break plane. Similar calculations show that these trends occur for longer cracks, i.e., $N > 1$.

5.3. Crack plane stress concentrations

Fig. 7 shows the crack plane tensile stresses in the fibers and matrix ahead of a 301 fiber break crack for values of ρ ranging from 0 to 2. Both the stress concentrations in the matrix and fiber shown in Fig. 7 are normalized by the stress concentration factor in the first intact fiber for the same crack size from the original Hedgepeth model, $\varepsilon_N^{\mathrm{H}}(0)/\varepsilon$. For plotting purposes, the fiber stresses are located at $s = 1, 2, \ldots$, and the matrix stresses are located at $(s - 1/2)$. Even for this relatively large crack size of $N = 301$, these results show that

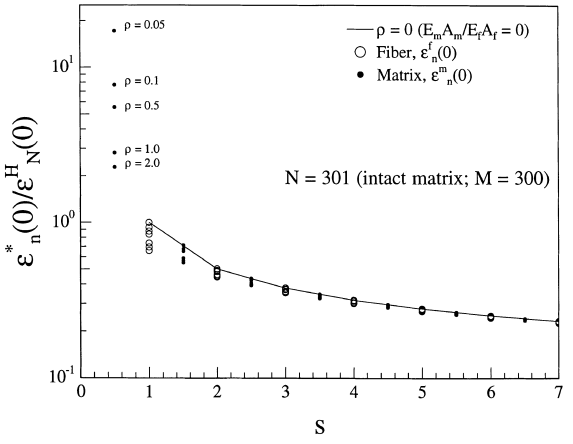

Fig. 7. The crack plane tensile stresses ahead of a row of $N = 301$ fiber breaks for various values of ρ. On the horizontal axis, the fiber nodes are at integers s and matrix nodes between fiber nodes s and $s + 1$ are at $s + 1/2$. On the vertical axis, the fiber stress (open circles) and matrix stress (solid circles) are normalized by the stress concentration factor, $\varepsilon_N^{\mathrm{H}}(0)/\varepsilon$, the calculated stress concentration factor in the first intact fiber ahead of N breaks in the case $\rho = 0$.

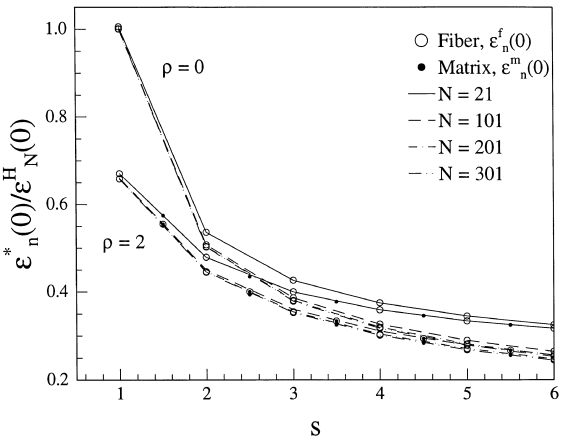

Fig. 8. The crack plane tensile stresses for various values of N and for $\rho = 0$ (Hedgepeth 2D shear-lag model) and $\rho = 2$. On the horizontal axis, the fiber nodes are at integers s and matrix nodes between fiber nodes s and $s + 1$ are at $s + 1/2$. On the vertical axis, the fiber stress (open circles) and matrix stress (solid circles) are normalized by the stress concentration factor, $\varepsilon_N^{\mathrm{H}}(0)/\varepsilon$.

the influence of ρ is more pronounced only within the first few fibers and matrix regions ($s < 3$) and gradually decays farther from the crack ($s \geqslant 3$). Similarly Fig. 8 shows the crack plane tensile stresses for various N for the two extreme values of ρ considered in this study, $\rho = 0$ and $\rho = 2$. As indicated, the fiber and matrix strain concentrations, Eqs. (28) and (29) are also normalized by the strain concentration factor $\varepsilon_N^{\mathrm{H}}(0)/\varepsilon$, where $\varepsilon_N^{\mathrm{H}}(0)/\varepsilon$ is the strain concentration factor in the first intact fiber ahead of an array of N breaks for $\rho = 0$ (i.e., the Hedgepeth limit).

For large values of N and $\rho = 0$, $\varepsilon_N^{\mathrm{H}}(0)/\varepsilon$ in the first intact fiber ahead of a row of N breaks is well approximated by (Beyerlein et al., 1996),

$$\frac{\varepsilon_N^{\mathrm{H}}(\xi = 0)}{\varepsilon} \approx \frac{\sqrt{\pi}}{2}\sqrt{N+1}, \quad N > 0, \tag{41}$$

which is analogous to the plane linear elasticity stress intensity factor ahead of a central crack. Eq. (41) proves to be very accurate as the error is about 6% for $N = 1$, 4% for $N = 2$ and is below 1% for $N \geqslant 10$, as shown in Table 1. Since $\varepsilon_N^{\mathrm{H}}(0)/\varepsilon \approx \sqrt{N}$, this normalization effectively scales out the dependence on N for $N \geqslant 101$ in Fig. 8. Also for fixed ρ, Figs. 7 and 8 uncover the initial

reduction in the crack plane tensile stress decay from the crack-tip with increases in ρ. Eventually beyond $s \geqslant 5$ and for all N, the relative differences between the decay behavior due to ρ become negligible.

5.4. Comparison with linear elasticity for large cracks

In this section, we study the performance of this shear-lag model at much larger length-scales. Specifically these results are compared to the Mode I linear elasticity solution for an orthotropic sheet containing a central crack of length 2c (Sih, 1981). In previous work, Beyerlein et al. (1996) demonstrated, that the Hedgepeth shear-lag model gives results for fiber tension and matrix shear consistent with this orthotropic continuum theory in both the long range and local behavior, at the length scale of the fiber diameter. Good agreement between the tensile stress was obtained given that the crack occupied 2/3rds of the matrix region flanked between the last broken and first intact fiber. However, the matrix shear stresses did not match so well, regardless of where the crack-tip was positioned. Similar comparisons are made in the framework of the present model with matrix and fiber nodes to see if agreement between shear and tensile stresses improve.

In order to compare the results with linear elasticity, composite properties used in this shear-lag model need to be related to elastic properties, E_L, E_T, ν_{LT}, and G_{LT}, required for a transversely isotropic continuum. For the axial stiffness, $E_L = E$ as before, where the rule-of-mixtures formula is used, i.e., $E_L = E = V_f E_f + (1 - V_f)E_m$. Also the shear modulus of the fiber is assumed infinite and therefore, for the in-plane composite shear modulus, $G_{LT} = G_m/(1 - V_f)$. In the present shear-lag method, the transverse displacements are neglected, and therefore to be consistent with this assumption, we set the overall composite transverse stiffness, E_T, to infinity and $\nu_{LT} = 0$. Second, we define the central crack $2c_N$ consisting of a row of N breaks in the composite lamina corresponding to the continuum crack 2c. In doing so, we consider the case where the crack-tip matrix regions are broken, and therefore, the crack extends up to the 1st intact fiber $s = 1$, as shown in Fig. 1. The composite crack is represented as

$$2c_N = (N-1)(W+D) + 2\left(\frac{D}{2} + W\right) \tag{42}$$

for $N \geqslant 1$.

Figs. 9–11 compare the fiber and matrix tensile strain concentrations $\varepsilon_n^f(x)/\varepsilon$ and $\varepsilon_n^m(x)/\varepsilon$ predicted by this shear-lag method and $\bar{\varepsilon}_{xx}/\varepsilon$ predicted by linear elasticity versus x, for $N = 301$ and intact fiber and matrix regions, $s = 1$ ($n = 151$) and $s = 2$ ($n = 152$). In the latter model, we average $\bar{\varepsilon}_{xx}/\varepsilon$ over the specified fiber or matrix region. Strain profiles in Figs. 9 and 10 are calculated using properties typical of a metal matrix fiber composite, where $V_f = 0.5$ ($W = D = 10$ μm), $E_m = 134$ GPa, $E_f = 400$ GPa, and thus, $\rho = 1/3$. Results in Figs. 11 and 12 are calculated for a typical polymer matrix fiber composite, where $V_f = 0.5$ ($W = D = 10$ μm), $E_m = 2.05$ GPa, $E_f = 98$ GPa and thus, $\rho = 0.0208$. In all cases, the average linear elasticity profiles achieve excellent agreement with the corresponding present shear-lag model axial profiles evaluated

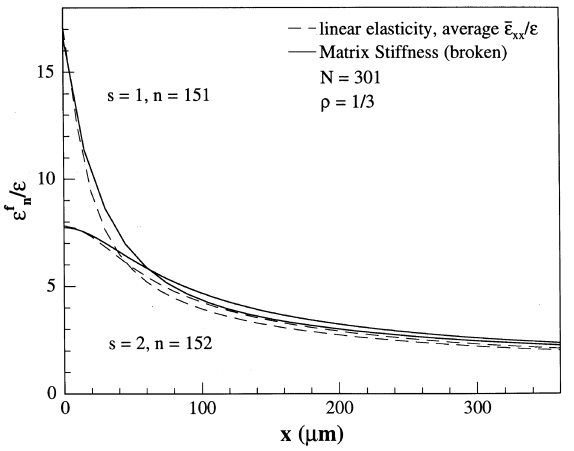

Fig. 9. Comparison between the fiber strain concentration profiles along the first ($s = 1$) and second ($s = 2$) intact fiber ahead of $N = 301$ fiber breaks (and $M = N + 1$ matrix breaks) and $\rho = 1/3$ (typical value for metal matrix fiber composite properties) as predicted by linear elastic fracture mechanics (dashed lines) and the present matrix stiffness shear-lag model (solid line). To be consistent with the shear-lag model, we assumed in the plane linear elasticity solution that the overall transverse stiffness is infinite. The linear elasticity profiles shown are averaged over the specified fiber diameter.

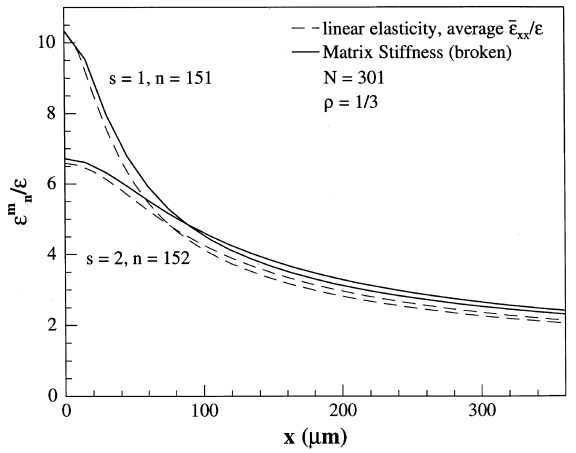

Fig. 10. Comparison between the matrix strain concentration profiles along the first ($s=1$) and second ($s=2$) intact matrix regions ahead of $N=301$ fiber breaks (and $M=N+1$ matrix breaks) and $\rho=1/3$ (typical value for metal matrix fiber composite properties) as predicted by plane linear elasticity (dashed lines) and shear-lag (solid line). To be consistent with the shear-lag model, we assumed in the plane linear elasticity solution that the overall transverse stiffness is infinite. The linear elasticity profiles shown are averaged over the specified matrix region.

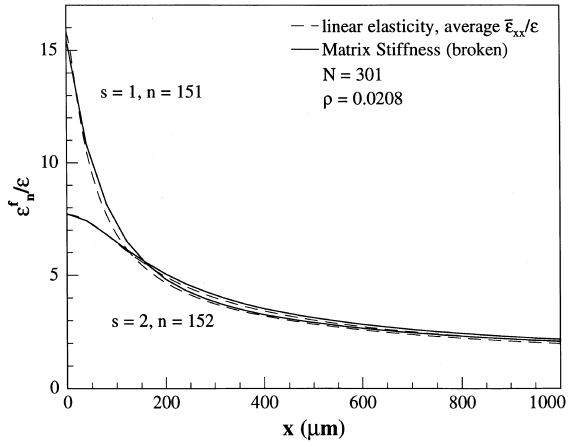

Fig. 11. Comparison between the fiber strain concentration profiles along the first ($s=1$) and second ($s=2$) intact fiber ahead of $N=301$ fiber breaks (and $M=N+1$ matrix breaks) and $\rho=0.0208$ (typical value for polymer matrix fiber composite properties) as predicted by plane linear elasticity (dashed lines) and shear-lag (solid line). To be consistent with the shear-lag model, we assumed in the plane linear elasticity solution that the overall transverse stiffness is infinite. The linear elasticity profiles shown are averaged over the specified fiber diameter.

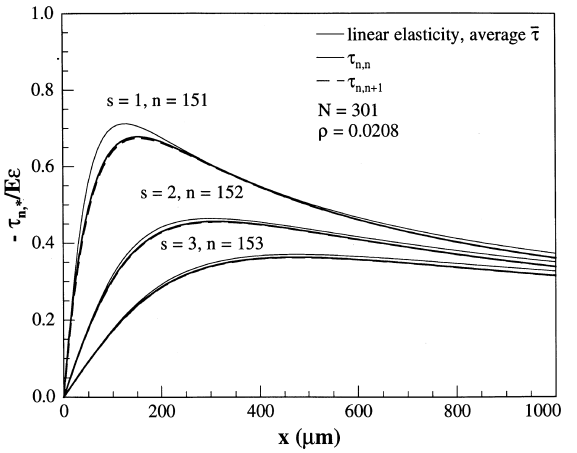

Fig. 12. Comparison between the matrix shear stress concentration profiles along the first, second, and third intact matrix regions ahead of $N=301$ fiber breaks (and $M=N+1$ matrix breaks) and $\rho=0.0208$ (typical value for polymer matrix fiber composite properties) as predicted by plane linear elasticity (dashed lines) and shear-lag (solid line). To be consistent with the shear-lag model, we assumed in the plane linear elasticity solution that the overall transverse stiffness is infinite. The linear elasticity profiles shown are averaged over the specified matrix region.

at fiber or matrix nodes with agreement improving as ρ decreases. For the same polymer matrix composite system, the normalized shear stresses in the first, second, and third intact matrix regions as predicted from linear elasticity and the present shear-lag model are compared in Fig. 12. Both $\tau_{n,n}/E\varepsilon$ and $\tau_{n,n+1}/E\varepsilon$ are shown for the shear-lag model and achieve much better agreement with the linear elasticity predictions $\bar{\tau}/E\varepsilon$, averaged over the matrix region, than the original Hedgepeth model. Based on several similar calculations, we expect similar agreement for all values of $N \geqslant 100$ and for a large range of ρ.

6. Conclusions

The shear-lag model and influence superposition technique developed here is an efficient computational tool for computing fiber and matrix stresses in simulations of fiber composites under tension or compression. Specifically, it has been formulated to compute axial stresses and

displacements in both the fiber and matrix around interacting, multiple fiber and matrix breaks in any general arrangement. Since computation time is tied to the number of breaks rather than composite size, it can provide quick recalculation in failure simulations as breaks occur and cracks form and extend, while retaining the physics at the microscale.

These results show a significant dependence on the fiber-to-matrix stiffness ratio, $\rho = E_m A_m / E_f A_f$, which couples the effects of two factors: the relative sizes and relative axial moduli of the fiber and matrix. These two effects are not captured in the original Hedgepeth shear-lag model, which corresponds to $\rho = 0$. The results presented here are computed for values of ρ in the range 0–2. In investigating the influence of ρ on stress transfer, we examined stress distributions produced by transverse cracks of various lengths N and studied two cases: case (i) where the matrix regions between the two broken fibers at the ends of the crack and the first intact fiber were intact and case (ii) where they were broken. In both cases, the peak fiber stress concentrations decrease and peak matrix stress concentrations increase as ρ increases for all N. Also, as the numbers of fiber breaks N increases, the change in peak stress concentration with change in ρ increases. However, even for the largest crack size studied here ($N = 301$), the relative differences in stress concentrations resulting from changes in ρ diminish beyond a few fibers ahead of the crack-tip. The results also show that significant differences in fiber stress occur between cases (i) and (ii). Apart from lower fiber stress concentrations, case (i) also leads to larger overstress lengths and a local rise in the fiber stress away from the break plane. Lastly, the fiber and matrix axial stress profiles obtained from linear elasticity and the present shear-lag model are compared. We find that the fiber and matrix axial stresses, and most significantly, the matrix shear stresses, predicted by this shear-lag model are consistent with those calculated by orthotropic linear elasticity (assuming $E_T = \infty$) and averaged across the corresponding fiber or matrix region.

The model developed by Ochiai et al. (1991) also yields similar results for fiber stress as seen in Fig. 4. However, in their formulation, the fiber strain in fibers beyond a fixed number (i.e., ±9 fibers) was assumed to be uniform. We find that their values are slightly higher than our predictions when the matrix is cut and slightly lower than our predictions when the matrix is intact. Similarly, compared to results from Rossettos and Shishesaz (1987) for $\rho = 0.176$ (or $\varepsilon = 0.088 = \rho/2$ in their work), and for a row of N breaks with broken crack-tip matrices within a 21 fiber composite, our results are slightly lower, with differences increasing with N. Lastly, trends seen in Fig. 4 are in agreement with recent peizospectroscopic measurements of fiber stress in situ in model composites, which show that as the interfiber spacing increases (or as ρ increases), the crack plane stress concentration in the immediate neighboring fiber decreases (Wagner et al., 1996; van den Heuvel et al., 1997; He et al., 1998; Beyerlein et al., 1998a, b).

For any value of $\rho \geqslant 0$, the present model can potentially treat a wide variety of composite material systems. One broad application would be for modeling failure in ceramic matrix and metal matrix composites with relatively strong interfaces and little or no interface debonding or matrix plasticity, such that failure evolution is dominated by multiple cracking of the matrix and fibers. In order to simulate the failure of a composite with a shear-lag model like the one presented here, potential failure sites must be placed along the fibers and matrix and their 'strengths' assigned. As uniform stress is applied to the composite, the site with the smallest strength will fail first, and stresses will be redistributed according to the shear-lag model stress analysis. The local stresses are then compared to the strengths at all other failure sites to see if they are overloaded. If sites are overloaded then they are broken and the stress is again redistributed. When no remaining sites are overloaded, then the far field stress is incremented and the process repeated until the composite reaches a maximum applied stress. For more detailed algorithms, see the works of Beyerlein and Phoenix (1997), Ibnabdeljalil and Curtin (1997), and Landis et al. (1998a, b). Finally with respect to more realistic modeling of composites, it is possible to develop a similar influence superposition technique for 3D fiber arrangements to reflect the axial and transverse stress carrying capacity of the

matrix and to include interfacial failure with various levels of sophistication.

Acknowledgements

IJB is grateful for the support provided at Los Alamos National Laboratory under a J.R. Oppenheimer Fellowship. CML was supported by a Regents Fellowship from the University of California. The authors would like to thank Professor Robert McMeeking for useful discussions on this topic.

References

Beyerlein, I.J., Phoenix, S.L., Sastry, A.M., 1996. Comparison of shear lag theory and continuum fracture mechanics for modeling fiber and matrix stresses in an elastic cracked composite lamina. Int. J. Solids Structures. 33, 2543–2574.

Beyerlein, I.J., Phoenix, S.L., 1996. Stress Concentrations Around Multiple Fiber Breaks in an Elastic Matrix with Local Yielding or Debonding using Quadratic Influence Superposition. J. Mech. Phys. Solids 44, 1997–2039.

Beyerlein, I.J., Phoenix, S.L., 1997. Statistics of fracture for an elastic notched composite lamina containing Weibull fibers. Part I: Features from Monte Carlo simulation and Part II: Probability models for crack growth. Engng. Fract. Mech. 57, 241–265 and 267–299.

Beyerlein, I.J., Phoenix, S.L., Raj, R., 1998a. Time evolution of stress redistributions around multiple fiber breaks in a composite with viscous and viscoelastic matrices. Int. J. Solids Structures 35, 3177–3211.

Beyerlein, I.J., Amer, M.S., Schadler, L.S., Phoenix, S.L., 1998b. New methodology for determining in situ fiber, matrix, and interface stresses in damaged multifiber composites. Sci. Engng. Comp. Mat. 7, 151–204.

Cook, R.D., Malkus, D.S., Plesha, M.E., 1974. Concepts and Applications of Finite Element Analysis, 3rd ed. John Wiley and Sons.

Eringen, A.C., Kim, B.S., 1973. Stress concentrations in filamentary composites with broken fibers. Princeton University, Tech. Rep. No. 36.

Fukuda, H., Chou, T.W., 1983. Stress-concentrations in a hybrid composite sheet. Journal of Applied Mechanics-Transactions of the ASME. 50, 845–848.

Fukuda, H., Kawata, K., 1976. On the Stress Concentration Factor in Fiberous Composites. Fiber Sci. Tech. 9, 189–203.

Goree, J.G., Gross, R.S., 1980. Stresses in a three-dimensional unidirectional composite containing broken fibers. Engng. Fract. Mech. 13, 395–405.

He, J., Clarke, D.R., 1995. Determination of the Piezospectroscopic Coefficients for Chromium-Doped Sapphire. J. Am. Ceram. Soc. 78, 1347–1353.

He, J., Beyerlein, I.J., Clarke, D.R., 1998. Load transfer from broken fibers in continuous fiber Al_2O_3-Al composites and dependence on local volume fraction. J. Mech. Phys. Solids, In Press.

Hedgepeth, J.M., 1961. Stress Concentration in Filamentary Structures. NASA TN D-822.

Hedgepeth, J.M., Van Dyke, P., 1967. Local Stress Concentration in Imperfect Filamentary Composite Materials. J. Compos. Mater. 1, 294–309.

Ibnabdeljalil, M., Curtin, W.A., 1997. Size effects on the strength of fiber-reinforced composites: localized load-sharing and associated size effects. Int. J. Solids Structures 34, 2649–2668.

Landis, C.M., McMeeking, R.M., 1998. Stress concentrations in composites with interface sliding, matrix stiffness, and uneven fiber spacing using shear lag theory. To appear in Int. J. Solids Structures.

Landis, C.M., McGlockton, M., McMeeking, R.M., 1998. An improved shear lag model for broken fibers in composites, To appear in J. Compos. Mater.

Landis, C.M., Beyerlein, I.J., McMeeking, R.M., 1998. Micromechanical simulation of the failure of fiber reinforced composites. submitted to J. Mech. Phys. Solids.

Mukunda, V.G., Dharani, L.R., 1993. A comparison of classical and consistent shear lag models for failure analysis of unidirectional composites. Engng. Fract. Mech. 45, 865–874.

Nagle, R.K., Saff, E.B., 1986. Fundamentals of Differential Equations, The Benjamin/Cummings Publishing Company, Inc., California.

Nairn, J.A., 1988. Fracture mechanics of unidirectional composites using the shear lag model I: Theory. J. Comp. Mat. 22, 561–588.

Nedele, M.R., Wisnom, M.R., 1994. Three dimensional finite element analysis of the stress concentration at a single fibre break. Comp. Sci. Tech. 51, 517–524.

Ochiai, S., Schulte, K., Peters, P.W.M., 1991. Strain concentration factors for fibers and matrix in unidirectional composites. Comp. Sci. Technol. 41, 237–256.

Press, W.H., Teukolsky, S.A., Vetterling, W.T., Flannery, B.P., 1992. Numerical Recipes in Fortran, The Art of Scientific Computing, 2nd ed. Cambridge University Press, New York.

Rossettos, J.N., Shishesaz, M., 1987. Stress Concentration in Fiber Composite Sheets Including Matrix Extension. J. Appl. Mech. 54, 723–724.

Sastry, A.M., Phoenix, S.L., 1993. Load redistribution near non-aligned fibre breaks in a two-dimensional unidirectional composite using break-influence superposition. J. Mat. Sci. Lett. 12, 1596–1599.

Schadler, L.S., Amer, M.S., Iskandarani, B., 1996. Experimental measurements of fiber/fiber interaction using Micro-Raman spectroscopy. Mech. Mater. 23, 205–216.

Sih, G.C., 1981. Cracks in Composite Materials. Martinus Nijhoff Publishers, Boston.

Suemasu, H., 1984. Probabilistic aspects of strength of unidirectional fibre-reinforced composites with matrix failure. J. Mat. Sci. 19, 574–584.

Van den Heuvel, P.W.J., Peijs, T., Young, R.J., 1997. Failure phenomena in two-dimensional multi-fibre microcomposites: 2. A Raman spectroscopic study of the influence of inter-fibre spacing on stress concentrations. Comp. Sci. Technol. 57, 899–912.

Van Dyke, P., Hedgepeth, J.M., 1969. Stress concentrations from single-filament failures in composite materials. Textile Res. J. 39, 618–626.

Wagner, H.D., Amer, M.S., Schadler, L.S., 1996. Fiber interactions in two dimensional composites by micro-Raman spectroscopy. J. Mater. Sci. 31, 1165–1173.

Zeng, Q.D., Wang, Z.L., Ling, L., 1997. A Study of the Influence of Interfacial Damage on Stress Concentration in Unidirectional Composites. J. Compos. Mater. 57, 129–135.

Zhou, S.J., Curtin, W.A., 1995. Failure of fiber composites: a lattice Green function model. Acta. Metall. Mater. 43, 3093–3104.

Zweben, C., 1974. An approximate method of analysis for notched unidirectional composities. Engng. Fract. Mech. 6, 1–10.